Oxygen reduction at thin dense $La_{0.52}Sr_{0.48}Co_{0.18}Fe_{0.82}O_{3-\delta}$ electrodes

Part I: Reaction model and faradaic impedance

Michel Prestat · Jean-François Koenig · Ludwig J. Gauckler

Abstract The faradaic impedance of oxygen reduction has been simulated for thin dense two-dimensional $La_{0.52}Sr_{0.48}Co_{0.18}Fe_{0.82}O_{3-\delta}$ electrodes in air at 600°C. The reaction model accounts for the defect chemistry of the ceramic films and includes bulk and surface pathways. It was demonstrated that the contribution of the surface pathway to the reaction was negligible due to the small length of triple phase boundary gas/electrode/electrolyte. The diffusion of oxygen in the bulk of $La_{0.52}Sr_{0.48}Co_{0.18}Fe_{0.82}O_{3-\delta}$ (LSCF) can be evidenced by measuring the polarization resistance as a function of the electrode thickness that ranged between 10 and 800 nm. When recorded as a function of the electrode potential and thickness, the frequency response exhibited features that were specific to the rate-determining steps of the reaction. The oxygen reduction mechanism and kinetics can therefore be identified by means of impedance spectroscopy. The faradaic impedances calculated for realistic values of the rate constants exhibited a noteworthy large faradaic capacitance.

Keywords Oxygen reduction · Solid oxide fuel cells · Dense films · LSCF · Faradaic impedance

M. Prestat (✉) · L. J. Gauckler
ETH-Zurich, Institute for Nonmetallic Inorganic Materials,
Wolfgang-Pauli-Strasse 10, HCI G531, Zurich 8093, Switzerland
e-mail: michel.prestat@mat.ethz.ch

J.-F. Koenig
Université Louis Pasteur, Laboratoire d'Électrochimie
et de Chimie Physique du Corps Solide, UMR 7177,
4 rue Blaise Pascal, Strasbourg 67070, France

1 Introduction

One major goal in solid oxide fuel cell (SOFC) research is to decrease the operating temperature in order to address the issues of running costs and long-term durability. The target temperature is below 600°C. Yet it is well known that the electrochemical activity of electrodes decreases with temperature and therefore it becomes more difficult to reach an acceptable cell performance. Alternative materials to the state-of-art high temperature (>800°C) strontium-doped lanthanum manganites ($La_xSr_{1-x}Mn_yO_3$, hereafter denoted LSM) are under investigation [1]. In the last decade, strontium- and iron-substituted lanthanum cobaltites, $La_xSr_{1-x}Co_yFe_{1-y}O_{3-\delta}$ (LSCF), have attracted much attention as suitable materials for intermediate temperature SOFC. LSCF is more electrocatalytically active than LSM towards the oxygen reduction reaction [2], LSCF has a similar electronic conductivity as LSM but exhibits better bulk transport properties of oxygen anions. A direct consequence of this mixed ionic-electronic behaviour is that oxygen reduction can take place along the surface of the LSCF grain as well as through the bulk of the electrode material. Both reaction pathways are in competition and can be simultaneously followed, depending on their kinetics. LSCF is known to form undesirable insulating phases such as strontium zirconate [3] when adjoining yttria-stabilized zirconia. Therefore LSCF is often associated to ceria based electrolyte, such as cerium-gadolinium oxide (CGO), because of chemical and thermal compatibility. LSCF is also compatible with CGO as regards the thermomechanical properties.

There is still debate around the oxygen reduction mechanism at mixed ionic-electronic electrodes in the literature [4]. Adler et al. brought forth a mechanism for oxygen reduction at porous $La_{0.6}Ca_{0.4}Co_{0.2}Fe_{0.8}O_{3-\delta}$ and

$La_{0.6}Sr_{0.4}Co_{0.2}Fe_{0.8}O_{3-\delta}$ electrodes [5]. The authors assumed the charge transfer step at the electrode/electrolyte interface to be facile and oxygen surface exchange as well as solid-state diffusion to be rate-determining. The modelling and experiments were carried out with symmetrical cells (i.e. at equilibrium only). The reaction mechanism did not involve any surface pathway. In contrast, Liu and Wu pointed out the importance of charge transfer at the electrode/electrolyte interface by measuring the equilibrium impedance of oxygen reduction at porous $La_{0.7}Sr_{0.3}Co_{0.7}Fe_{0.3}O_{3-\delta}$ electrodes with various electrolyte materials [6]. The nature of the latter markedly affected the area specific resistance (ASR) of the reaction. Sirman et al. compared the impedance of porous and dense $La_{0.6}Sr_{0.4}Co_{0.2}Fe_{0.8}O_{3-\delta}$ electrodes [7]. The 1 µm thick dense electrode showed a significantly larger polarization resistance. Those findings contradict the results reported by Steele and Bae [8] who measured the influence of a dense $La_{0.6}Sr_{0.4}Co_{0.2}Fe_{0.8}O_{3-\delta}$ layer (~1 µm thick) placed between a porous LSCF film and a CGO electrolyte. The ASR of the electrode with the dense film was 2 to 3 times lower. Brichzin et al. used geometrically well-defined dense $(La_{0.8}Sr_{0.2})_{0.92}MnO_3$ microelectrodes and measured their impedance as a function of the diameter d [9]. The polarization resistance was found to be dependant on d^{-2}. The authors concluded that the bulk pathway was dominant in contrast to the common view that LSM favours oxygen reduction via the surface pathway. In a continuing work, Baumann et al. investigated the impedance of thin microstructured $La_{0.6}Sr_{0.4}Co_{0.8}Fe_{0.2}O_{3-\delta}$ electrodes and drew the same conclusions as Brichzin as regards the preferred reaction bulk pathway [10]. However in both studies, the electrodes exhibited large area specific resistivity (~400 Ω. cm^2 for LSM at 800°C and 10 $\Omega.cm^2$ for LSCF at 750°C). As for LSM, this could be explained by the fact that the geometry of the electrodes (the diameter was much greater than the thickness) forced the reaction to occur through the bulk of the LSM whose rates of oxygen transport are known to be poor [11, 12]. The high ASR values of LSCF were not discussed. Recently Esquirol et al. stressed the importance of oxygen nonstoichiometry by studying the properties of the $La_{0.6}Sr_{0.4}Co_{0.2}Fe_{0.8}O_{3-\delta}$ (porous)/CGO interface [13]. It was claimed that, above 600°C, LSCF is oxygen-nonstoichiometric and exhibits mixed ionic-electronic properties which enhances the contribution of the bulk pathway. Below this temperature, the LSCF is stoichiometric. The absence of oxygen vacancies for bulk diffusion favours the promotion of the surface pathway.

In order to comprehensively interpret experimental electrochemical impedance spectra, it is important to know the relation between the reaction mechanism and the frequency response. In this work the faradaic impedance of oxygen reduction at thin dense $La_{0.52}Sr_{0.48}Co_{0.18}Fe_{0.82}O_{3-\delta}$

electrodes in air at 600°C has been simulated as a function of electrode overpotential and film thickness for various kinetic situations, i.e. for different rate-determining steps (rds) of the reaction using state-space modelling [14, 15]. In a companion paper [16], using a numerical optimization process, the simulated reaction impedance has been compared to experimental data produced with geometrically-well defined LSCF films prepared by pulsed laser deposition and structured with photolithography.

2 Composition and defect chemistry of LSCF

2.1 Composition

In order to calculate the kinetics of oxygen reduction bulk pathway, it is first necessary to know the concentration of the various elements of the $La_{0.52}Sr_{0.48}Co_{0.18}Fe_{0.82}O_{3-\delta}$ perovskite involved in the reaction at equilibrium, i.e. the concentration of oxygen, c_{to}, the concentration of B sites, c_{tc}, as well as the level of strontium substitution. These values were calculated from nonstoichiometry (δ), density (ρ) and thermal expansion data reported in the literature (Table 1).

2.2 Defect chemistry

In order to account for the defect chemistry of the LSCF perovskite, a simple model, based on the work of Wang [17], has been chosen. The Fe^{n+} and Co^{n+} ions ($2 \leq n \leq 4$) are thought to behave similarly and to be distributed randomly on the B sites of the perovskite. Iron and cobalt cations were treated as equal. In what follows, the B sites are denoted as Co sites. In the Kröger–Vink notation, $Co_{Co}^{\bullet}(Co^{4+})$ and $Co_{Co}'(Co^{2+})$ respectively represent a hole and an electron localized on a B site. The Sr^{2+} cations sit on the La sites because of similar ionic radii. This reaction is

Table 1 Concentration of the key-species in $La_{0.52}Sr_{0.48}Co_{0.18}Fe_{0.82}O_{3-\delta}$ at 600°C in air under equilibrium.

Key-species	Values
δ [21]	0.02
M (g mol^{-3})	218.4
ρ_{25} at 25°C (g cm^{-3})	6.25
ρ at 600°C (g cm^{-3})	6.07
[Sr] (mol L^{-1})	12.7
[O] = c_{to} (mol L^{-1})	79.2
$[V_o^{\bullet\bullet}]$ (mol L^{-1})	0.528
[Co]+[Fe] = c_{tc} (mol L^{-1})	26.4

The density at room temperature has been linearly interpolated from the values obtained at various strontium contents [18–20]. The density at 600°C was calculated by taking into account the linear expansion between room temperature to the final temperature [20].

believed to proceed completely. The substitution of La^{3+} by Sr^{2+} creates a fully ionised acceptor level (Sr'_{La}), whose charge is compensated by the generation of holes ($Co^{\cdot}_{Co}$) and oxygen vacancies ($V^{\cdot\cdot}_o$). The concentration of Sr'_{La} is assumed to be uniform throughout the LSCF layer and to remain constant out of equilibrium.

The disproportionation reaction is taken into account:

$$2Co^x_{Co} \overset{K_\alpha}{\rightleftharpoons} Co'_{Co} + Co^{\cdot}_{Co} \qquad (1)$$

If K_α is known, the concentrations of the cobalt species are tied to $[V^{\cdot\cdot}_o]$ by means of the following three equations:

Conservation of Co:

$$\left[Co'_{Co}\right] + \left[Co^{\cdot}_{Co}\right] + \left[Co^x_{Co}\right] = c_{tc} \qquad (2)$$

Electroneutrality (see assumptions, Section 4):

$$\left[Sr'_{La}\right] + \left[Co'_{Co}\right] = 2\left[V^{\cdot\cdot}_o\right] + \left[Co^{\cdot}_{Co}\right] \qquad (3)$$

Disproportionation equation:

$$K_\alpha = \frac{\left[Co'_{Co}\right]\left[Co^{\cdot}_{Co}\right]}{\left[Co^x_{Co}\right]^2} \qquad (4)$$

By solving the Eqs. 2, 3 and 4, one gets

$$\left[Co^{\cdot}_{Co}\right] = \frac{4K_\alpha(c_{tc} + c) - c - \sqrt{c^2 + 4K_\alpha(c^2_{tc} - c^2)}}{8K_\alpha - 2}$$
$$= \left[Co^{\cdot}_{Co}\right]_{eq} \qquad (5)$$

$$\left[Co^x_{Co}\right] = \frac{-c_{tc} + \sqrt{c^2 + 4K_\alpha(c^2_{tc} - c^2)}}{4K_\alpha - 1} = \left[Co^x_{Co}\right]_{eq} \qquad (6)$$

$$\left[Co'_{Co}\right] = \frac{4K_\alpha(c_{tc} - c) + c - \sqrt{c^2 + 4K_\alpha(c^2_{tc} - c^2)}}{8K_\alpha - 2}$$
$$= \left[Co'_{Co}\right]_{eq} \qquad (7)$$

Table 2 Concentration of the cobalt species (B sites) in $La_{0.52}Sr_{0.48}Co_{0.18}Fe_{0.82}O_{3-\delta}$ at 600°C in air (δ=0.02).

Cobalt species	Values
K_α (extrapolated value) [17]	$3.63 \ 10^{-4}$
$\left[Co^{\cdot}_{Co}\right]_{eq}$ (mol L^{-1})	11.6
$\left[Co^x_{Co}\right]_{eq}$ (mol L^{-1})	14.8
$\left[Co'_{Co}\right]_{eq}$ (mol L^{-1})	$6.96 \ 10^{-3}$

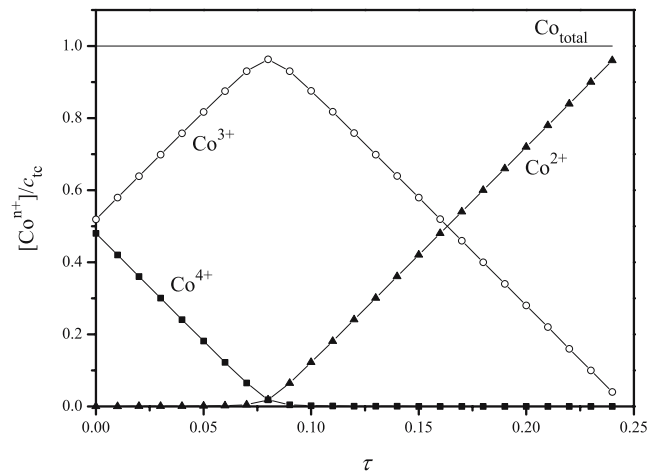The calculations used the strontium doping level and the oxygen nonstoichiometry of Table 1.

Fig. 1 Concentration of the cobalt species in $La_{0.52}Sr_{0.48}Co_{0.18}Fe_{0.82}O_{3-\delta}$ as a function of the level of oxygen nonstoichiometry ($\tau = [V^{\cdot\cdot}_o]/c_{to}$). These plots have been calculated using Eqs. 5, 6 and 7) The defect chemistry model is not valid above τ=0.24 (when LSCF is completely reduced)

with

$$c = \left[Sr'_{La}\right] - 2\left[V^{\cdot\cdot}_o\right] \qquad (8)$$

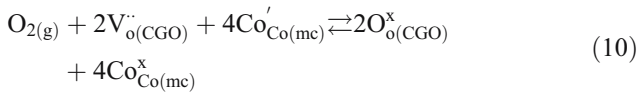The equilibrium concentration of the cobalt species can be found in Table 2.

Figure 1 shows the concentration of the three cobalt species as a function of the vacancy ratio τ ($\tau = [V^{\cdot\cdot}_o]/c_{to}$) according to Eqs. 5, 6 and 7. At equilibrium, LSCF is a p-type semiconductor and the couple Co^{3+}/Co^{4+} is abundant. For $0 < \tau < 0.08$, the holes are replaced by the oxygen vacancies to compensate the negatively charged Sr'_{La}. Accordingly the concentration of Co^{3+} increases till a maximum at τ=0.08 that corresponds to the quasi-disappearance of the Co^{4+} as well as the onset of the Co^{2+} concentration increase. At τ=0.24, the LSCF is completely reduced. This value of the vacancy concentration constitutes the limit of applicability of this defect chemistry model. At $\tau \geq 0.25$, the positive charges due to the oxygen vacancies cannot be fully compensated by the negative defects Sr'_{La} and Co'_{Co}. Hence electroneutrality is not obeyed anymore. In this work, the values of τ are restricted to the range [0–0.24].

3 Reaction model

In the Kröger–Vink notation, the oxygen reduction at the gas/electrode/electrolyte interface can be written:

$$O_{2(g)} + 2V^{\cdot\cdot}_{o(CGO)} + 4Co^x_{Co(mc)} \rightleftharpoons 2O^x_{o(CGO)}$$
$$+ 4Co^{\cdot}_{Co(mc)} \qquad (9)$$
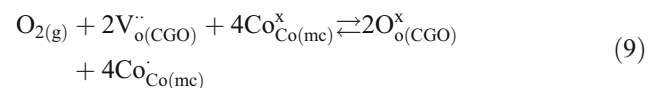
when the LSCF is in the oxidized state, or

$$O_{2(g)} + 2V_{o(CGO)}^{\cdot\cdot} + 4Co_{Co(mc)}' \rightleftarrows 2O_{o(CGO)}^{x} \\ + 4Co_{Co(mc)}^{x} \tag{10}$$

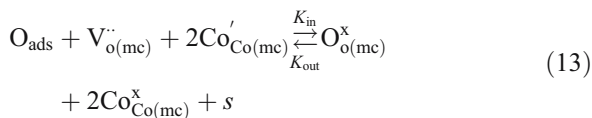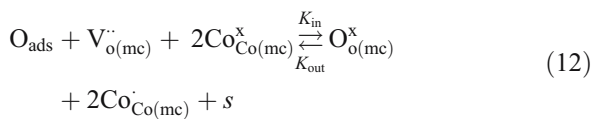when the LSCF is in the reduced state.

The subscripts (g), (mc) and (CGO) represent the gas phase, the mixed conductor (LSCF) and the electrolyte (CGO), respectively. The oxygen reduction mechanism investigated in this work is depicted in Fig. 2.

In the Kröger–Vink notation, the bulk pathway can be written as follows:

Adsorption:

$$O_{2(g)} + 2s \underset{K_{des}}{\overset{K_{ads}}{\rightleftarrows}} 2O_{ads} \tag{11}$$

Oxygen exchange (incorporation) between the adsorbate and the LSCF:

$$O_{ads} + V_{o(mc)}^{\cdot\cdot} + 2Co_{Co(mc)}^{x} \underset{K_{out}}{\overset{K_{in}}{\rightleftarrows}} O_{o(mc)}^{x} \\ + 2Co_{Co(mc)}^{\cdot} + s \tag{12}$$

$$O_{ads} + V_{o(mc)}^{\cdot\cdot} + 2Co_{Co(mc)}' \underset{K_{out}}{\overset{K_{in}}{\rightleftarrows}} O_{o(mc)}^{x} \\ + 2Co_{Co(mc)}^{x} + s \tag{13}$$

with s being in a non-occupied adsorption site at the surface of the LSCF.

Diffusion of oxygen vacancies:

$$V_{o(mc)}^{\cdot\cdot} \overset{D}{\rightarrow} V_{o(mc)}^{\cdot\cdot} \tag{14}$$

Oxygen exchange (charge transfer) at the LSCF/CGO interface

$$O_{o(mc)}^{x} + V_{o(CGO)}^{\cdot\cdot} \underset{K_{bb}}{\overset{K_{fb}}{\rightleftarrows}} V_{o(mc)}^{\cdot\cdot} + O_{o(CGO)}^{x} \tag{15}$$
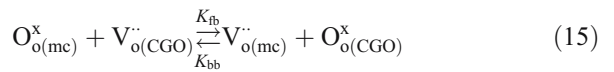
Similarly the surface pathway can be written as follows:

Adsorption:

$$O_{2(g)} + 2s \underset{K_{des}}{\overset{K_{ads}}{\rightleftarrows}} 2O_{ads} \tag{16}$$

Oxygen exchange (incorporation) between the adsorbate and the LSCF:

$$O_{ads} + V_{o(mc)}^{\cdot\cdot} + 2Co_{Co(mc)}^{x} \underset{K_{out}}{\overset{K_{in}}{\rightleftarrows}} O_{o(mc)}^{x} + 2Co_{Co(mc)}^{\cdot} \\ + s \tag{17}$$

$$O_{ads} + V_{o(mc)}^{\cdot\cdot} + 2Co_{Co(mc)}' \underset{K_{out}}{\overset{K_{in}}{\rightleftarrows}} O_{o(mc)}^{x} \\ + 2Co_{Co(mc)}^{x} + s \tag{18}$$
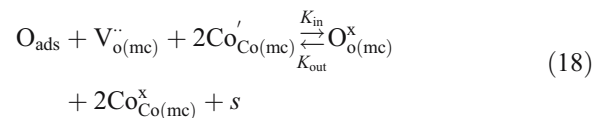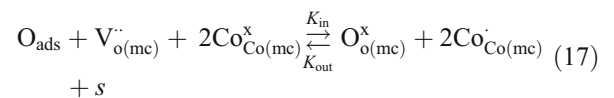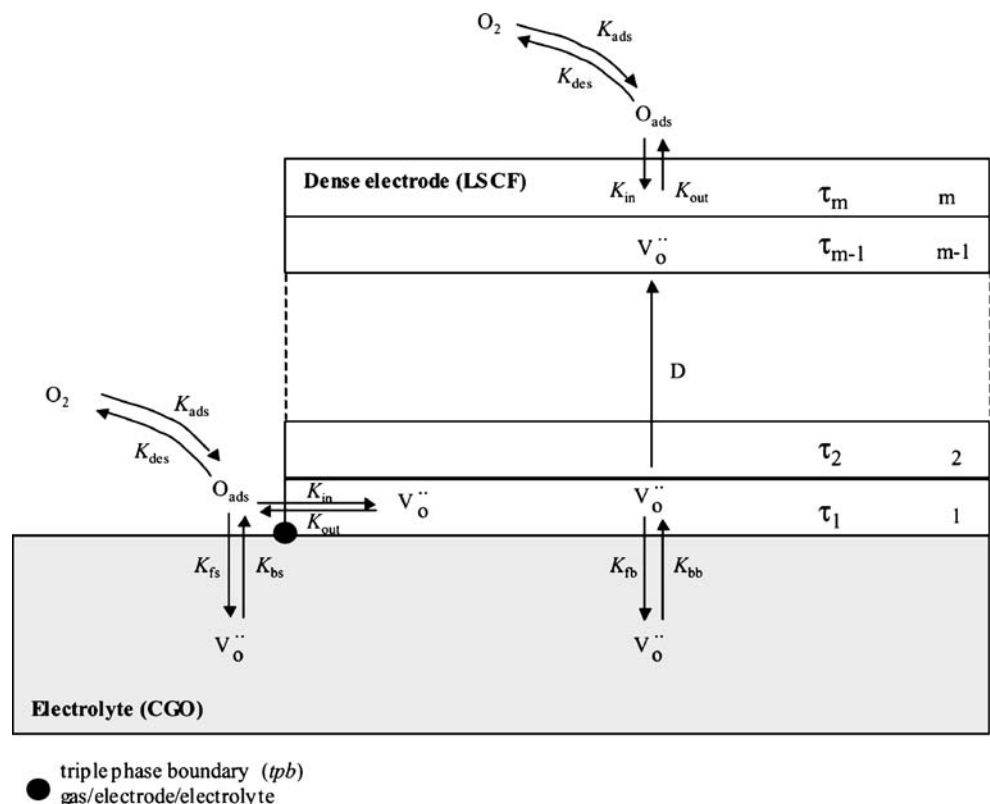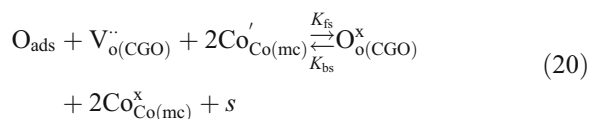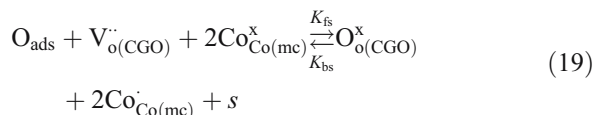
Fig. 2 Model for oxygen reduction mechanism including bulk and surface pathways. The rate constants refer to Eqs. 9, 10, 11, 12, 13, 14, 15, 16, 17, 18, 19 and 20. The segmentation of the LSCF layer allows for the numerical implementation of the diffusion process in the model. The state variable τ_i is defined in Section 5.1

Charge transfer at the *tpb*:

$$O_{ads} + V_{o(CGO)}^{\cdot\cdot} + 2Co_{Co(mc)}^{x} \underset{K_{bs}}{\overset{K_{fs}}{\rightleftharpoons}} O_{o(CGO)}^{x}$$
$$+ 2Co_{Co(mc)}^{\cdot} + s \qquad (19)$$

$$O_{ads} + V_{o(CGO)}^{\cdot\cdot} + 2Co_{Co(mc)}^{'} \underset{K_{bs}}{\overset{K_{fs}}{\rightleftharpoons}} O_{o(CGO)}^{x}$$
$$+ 2Co_{Co(mc)}^{x} + s \qquad (20)$$

All the rate constants of the model (K_{ads}, K_{des}, K_{in}, K_{out}, D, K_{fb}, K_{bb}, K_{fs} and K_{bs}) are independent of the oxygen concentration in the LSCF. The electrochemical rate constants K_{fb}, K_{bb}, K_{fs} and K_{bs} are dependant of the electrode potential. For reactions where the B sites are involved (see reactions (19) and (20) for instance), it is believed that the rate constants are identical regardless of the involved redox couple ($Co_{Co}^{\cdot}/Co_{Co}^{x}$ or $Co_{Co}^{x}/Co_{Co}^{'}$).

In order to numerically implement the bulk diffusion of oxygen vacancies in the model, the thickness, d, of the LSCF film has been segmented in m compartments of equal length, l (see Fig. 2):

$$d = ml \qquad (21)$$

4 Model assumptions

The aim of this work is to provide a mechanistic model that can be used in practice for the identification of the oxygen reduction mechanism at $La_{0.52}Sr_{0.48}Co_{0.18}Fe_{0.82}O_{3-\delta}$ films and the assessment of the kinetics when comparing simulated and experimental data with a numerical optimization process [16]. Modelling this kind of is very challenging since it requires many parameters that are still poorly known (mainly rate constants), a fortiori for thin films. In order to keep the calculation costs of the numerical optimization process, the treatment of this complex reaction model has been simplified by making the following assumptions:

(1) In air, the electrolyte (CGO) is a purely ionic conductor (ionic transference number ~ 1). Consequently the concentrations of $V_{o}^{\cdot\cdot}$ and O_{o}^{x} in the electrolyte remains invariant out of equilibrium.

(2) The square-shaped LSCF film is dense and thin, i.e. its width (3 mm) is much bigger than its thickness (<800 nm). The LSCF film can be seen as a two-dimensional object. As schematically depicted in Fig. 3, the incorporation of oxygen in the LSCF through the planes (*yz*) and (*xz*) is kinetically neglected. The oxygen reduction process is seen as a one dimensional process along the *z* axis. (No
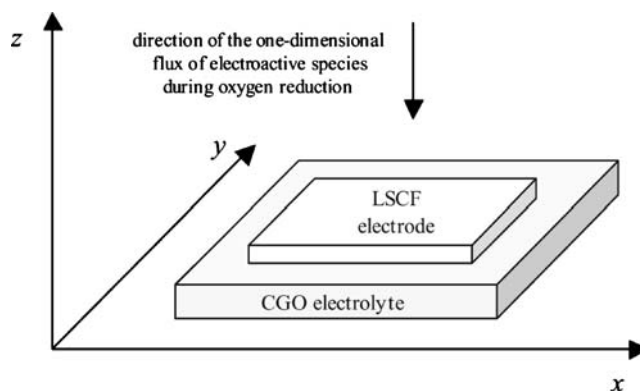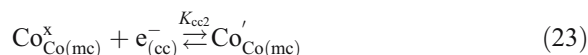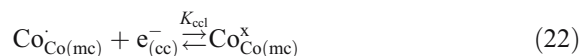
Fig. 3 Schematic representation of the orientation of the thin LSCF film. The film is considered as two-dimensional for its thickness is much smaller than its width (see assumption (2))

variation of electroactive species along the *x* and *y* axis are taken into account).

(3) In this simulation work, we consider a virtual current collector (CC) located on top of the electrode. The CC does not impede oxygen adsorption on the surface of the LSCF and allows for a uniform potential distribution in the electrode. The transfer of charge between the CC and the LSCF is considered as facile. Therefore the voltage difference at the LSCF/CC interface is constant regardless of the current. The value of the contact resistance is low and the capacitive effect at the LSCF/CC interface is ignored.

(4) The transfer of charge between the CC and the LSCF is infinitely fast and therefore remains at quasi-equilibrium. In the case of an electronic conducting CC, this can be written as follows:

$$Co_{Co(mc)}^{\cdot} + e_{(cc)}^{-} \overset{K_{cc1}}{\rightleftharpoons} Co_{Co(mc)}^{x} \qquad (22)$$

$$Co_{Co(mc)}^{x} + e_{(cc)}^{-} \overset{K_{cc2}}{\rightleftharpoons} Co_{Co(mc)}^{'} \qquad (23)$$

with the subscript (*cc*) representing the current collector and K_{cc1} and K_{cc2} the equilibrium constants of the reactions.

This leads to

$$\frac{K_{cc2}}{K_{cc1}} = \frac{[Co_{Co}^{'}]_m [Co_{Co}^{\cdot}]_m}{[Co_{Co}^{x}]_m^2} = K_\alpha \qquad (24)$$

In the compartment m, the fast transfer of charge between the LSCF and the CC maintains the disproportionation at quasi-equilibrium (Eq. 4).

(5) At the LSCF/CC and LSCF/CGO interfaces, the thickness of the space charge layers is believed to be small (less than a unit cell) due to the high concentration of mobile species (oxygen vacancies,

holes and electrons). Local electroneutrality prevails in the LSCF film. The gradient of electrical potential within the LSCF layer is negligible. The transport of oxygen vacancies is carried out by diffusion.

(6) To the best of our knowledge, no value of the dielectric constant of LSCF has been reported in the literature. It is assumed to be sufficiently small to ignore bulk polarization and displacement current in the AC mode.

(7) At equilibrium, the defect chemistry (and notably the oxygen nonstoichiometry δ) remains unchanged when the LSCF film is brought into contact with the electrolyte and the CC.

(8) When a current flows through the LSCF electrode, the disproportionation reaction remains at quasi-equilibrium and electroneutrality is obeyed in the whole LSCF film. Consequently the defect chemistry described in Section 2 is also valid out of equilibrium.

(9) The incorporation of oxygen in the LSCF is chemical in nature and does not involve any charge transfer across the LSCF/gas interface. The charge transfer steps of the present reaction mechanism are localized at the LSCF/CGO interface as well as at the tpb.

(10) The adsorption kinetics is identical at the tpb and all over the surface of the LSCF.

(11) The surface diffusion of adsorbed oxygen is considered as slow and therefore kinetically negligible. When oxygen follows the surface pathway, it is adsorbed and reduced directly at the tpb.

(12) Gas phase diffusion of molecular oxygen is neglected at the oxygen partial pressure used in this study (0.21 atm).

(13) In the bulk of the LSCF electrode, the bulk diffusion of oxygen occurs via oxygen vacancies only. The flux of electronic species (and therefore ambipolar diffusion) at high frequencies has been neglected. The relevance of this assumption as well as potential refinements are discussed in [16]. The diffusion coefficient D is seen as independent of the oxygen vacancy concentration. The role of interstitial sites has been ignored as well.

(14) Due to the geometry of the film (width $\gg$ thickness), the vacancy concentration is only determined by the bulk pathway kinetics taking place along the z axis and is not influenced by the oxygen incorporation reaction taking place on the (xz) and (yz) planes (see Figs. 2 and 3). In contrast, the concentration of adsorbed oxygen is affected by the oxygen content of the LSCF film. This is particularly noticeable at the tpb (see Eq. 40).

5 State-space model

5.1 State variables

For the bulk pathway, an oxygen vacancy ratio, τ_i, has been defined for each compartment of the LSCF film (see Fig. 2):

$$\left[V_o^{..}\right]_i = \tau_i c_{to} \tag{25}$$

$$\left[O_o^x\right]_i = (1 - \tau_i) c_{to} \tag{26}$$

Similarly, the concentration of adsorbed species has been expressed via the oxygen surface coverage, x_i, as follows:

$$[O_{ads}]_i = N x_i \tag{27}$$

$$[s]_i = N(1 - x_i) \tag{28}$$

where N is the surface concentration of adsorption sites.

Both τ_i and x_i are comprised between 0 and 1. The components of the vector $[x, x_{tpb}, \tau_1, \tau_2 ..., \tau_m]$, with x and x_{tpb} being the surface coverages of the compartment m and at the tpb, respectively, constitute the state variables of the present reaction model.

5.2 Diffusion

The implementation of the second Fick's law is numerically achieved with a finite difference approach. The time derivative of $\left[V_o^{..}\right]_i$ due to diffusion can be written as:

$$\left(\frac{\partial\left[V_o^{..}\right]_i}{\partial t}\right)_{dif} = \frac{J_{i-1,i} - J_{i,i+1}}{l_i} \tag{29}$$

where $J_{i-1,i}$ corresponds to the flux of adsorbed oxygen from compartment $i-1$ to the compartment i. The flux $J_{i-1,i}$ is proportional to the oxygen vacancy gradient between two adjacent compartments. By using a central difference approximation, one writes:

$$J_{i-1,i} = D \frac{\left[V_o^{..}\right]_{i-1} - \left[V_o^{..}\right]_i}{\frac{l_{i-1}}{2} + \frac{l_i}{2}} \tag{30}$$

where D is the diffusion coefficient of oxygen vacancies.

By substitution of Eqs. 25 and 30 into Eq. 29, the general form of the diffusion becomes:

$$\left(\frac{\partial \tau_i}{\partial t}\right)_{dif} = \frac{2D}{l_i}\left(\frac{\tau_{i-1}}{l_{i-1} + l_i} - \tau_i\left(\frac{1}{l_{i-1} + l_i} + \frac{1}{l_i + l_{i+1}}\right) + \frac{\tau_{i+1}}{l_i + l_{i+1}}\right) \tag{31}$$

5.3 Bulk pathway

At the surface of the LSCF (interface between compartment m and the gas phase), according to Eqs. 11, 12 and 13, the state equation of x is written

$$
\begin{aligned}
\frac{dx}{dt} = {} & 2K_{ads}p_{O_2}N(1-x)^2 - 2K_{des}Nx^2 \\
& - K_{in}xc_{to}\tau_m\left(\left[Co_{Co}^x\right]_m^2 + \left[Co_{Co}^{'}\right]_m^2\right) \\
& + K_{out}(1-x)c_{to}(1-\tau_m)\left(\left[Co_{Co}^x\right]_m^2 + \left[Co_{Co}^{\cdot}\right]_m^2\right)
\end{aligned}
\tag{32}
$$

In the compartment m, the bulk diffusion of oxygen vacancies is blocked (i.e. $l_{m+1}=\infty$). By taking this boundary condition into account and according to Eqs. 12, 13, 14, 21 and 31, the state equation of τ_i is written

$$
\begin{aligned}
\frac{d\tau_m}{dt} = {} & \frac{m^2D}{d^2}(\tau_{m-1} - \tau_m) \\
& + \frac{m}{d}\Bigg(-K_{in}Nx\tau_m\left(\left[Co_{Co}^x\right]_m^2 + \left[Co_{Co}^{'}\right]_m^2\right) \\
& + K_{out}N(1-x)(1-\tau_m)\left(\left[Co_{Co}^x\right]_m^2 + \left[Co_{Co}^{\cdot}\right]_m^2\right)\Bigg)
\end{aligned}
\tag{33}
$$

In the inner compartments ($1 < i < m$), only bulk diffusion of vacancies occurs. By using Eqs. 21 and 31, the state equation of τ_i is

$$
\frac{d\tau_i}{dt} = \frac{2m^2D}{d^2}\left(\frac{1}{2}\tau_{i-1} - \tau_i + \frac{1}{2}\tau_{i+1}\right)
\tag{34}
$$

At the interface LSCF/CGO (compartment 1), the bulk diffusion of oxygen vacancies is blocked (i.e. $l_0=\infty$). By taking this boundary condition into account and according to Eqs. 14, 15, 21 and 31, the state equation of τ_1 is written

$$
\frac{d\tau_1}{dt} = -\frac{m^2D}{d^2}(\tau_1 - \tau_2) + \frac{m}{d}(K_{fb}(1-\tau_1) - K_{bb}\tau_1)
\tag{35}
$$

with

$$
K_{fb} = k_{fb}e^{-2\alpha fE}
\tag{36}
$$

$$
K_{bb} = k_{bb}e^{2(1-\alpha)fE}
\tag{37}
$$

$$
f = \frac{F}{RT}
\tag{38}
$$

with E being the potential of the electrode, α the charge transfer coefficient, F the Faraday constant, R the gas constant and T the temperature. The pre-exponential factors k_{fb} and k_{bb} are independent of τ_1 and E.

The bulk contribution, j_b, to the faradaic current density is

$$
j_b = 2Fc_{to}(-K_{fb}(1-\tau_1) + K_{bb}\tau_1)
\tag{39}
$$

5.4 Surface pathway

At the tpb, according to Eqs. 16, 17, 18, 19 and 20, the state equation of x_{tpb} is written

$$
\begin{aligned}
\frac{dx_{tpb}}{dt} = {} & 2K_{ads}p_{O_2}N\left(1 - x_{tpb}\right)^2 - 2K_{des}Nx_{tpb}^2 \\
& - x_{tpb}\left(\left[Co_{Co}^x\right]_1^2 + \left[Co_{Co}^{'}\right]_1^2\right)(K_{in}c_{to}\tau_1 + K_{fs}) \\
& + \left(1 - x_{tpb}\right)\left(\left[Co_{Co}^x\right]_1^2 + \left[Co_{Co}^{\cdot}\right]_1^2\right) \\
& \quad (K_{out}c_{to}(1-\tau_1) + K_{bs})
\end{aligned}
\tag{40}
$$

with

$$
K_{fs} = k_{fs}e^{-2\alpha fE}
\tag{41}
$$

$$
K_{bs} = k_{bs}e^{2(1-\alpha)fE}
\tag{42}
$$

The pre-exponential factors k_{fs} and k_{bs} are independent of τ_1 and E.

The surface contribution, j_s, to the faradaic current density is

$$
\begin{aligned}
j_s = K_s\Bigg(& -K_{fs}x_{tpb}\left(\left[Co_{Co}^x\right]_1^2 + \left[Co_{Co}^{'}\right]_1^2\right) \\
& + K_{bs}\left(1 - x_{tpb}\right)\left(\left[Co_{Co}^x\right]_1^2 + \left[Co_{Co}^{\cdot}\right]_1^2\right)\Bigg)
\end{aligned}
\tag{43}
$$

whereby K_s is a constant that represents the charge (per unit of surface area) of the tpb area fully covered by oxygen being incorporated into the electrolyte.

The overall current density j is

$$
\begin{aligned}
j = j_b + j_s = {} & 2Fc_{to}(-K_{fb}(1-\tau_1) + K_{bb}\tau_1) \\
& + K_s\Bigg(-K_{fs}x_{tpb}\left(\left[Co_{Co}^x\right]_1^2 + \left[Co_{Co}^{'}\right]_1^2\right) \\
& + K_{bs}\left(1 - x_{tpb}\right)\left(\left[Co_{Co}^x\right]_1^2 + \left[Co_{Co}^{\cdot}\right]_1^2\right)\Bigg)
\end{aligned}
\tag{44}
$$

The Eqs. 32, 33, 34, 35, 40 and 44 constitute the state-space model. According to assumption (8), the concentrations $\left[Co_{Co}^{\cdot}\right]_i$, $\left[Co_{Co}^x\right]_i$ and $\left[Co_{Co}^{'}\right]_i$ have the same form as in Eqs. 5, 6 and 7 and are tied to τ_i by the relation

$$
c_i = \left[Sr_{La}^{'}\right] - 2c_{to}\tau_i
\tag{45}
$$

5.5 Equilibrium

At equilibrium, there is no gradient of concentration within the LSCF film. Therefore in every compartment:

$$\left[\text{Co}_{\text{Co}}^{\cdot}\right]_i = \left[\text{Co}_{\text{Co}}^{\cdot}\right]_{\text{eq}} \tag{46}$$

$$\left[\text{Co}_{\text{Co}}^{\text{x}}\right]_i = \left[\text{Co}_{\text{Co}}^{\text{x}}\right]_{\text{eq}} \tag{47}$$

$$\left[\text{Co}_{\text{Co}}^{\text{x}}\right]_i = \left[\text{Co}_{\text{Co}}^{\text{x}}\right]_{\text{eq}} \tag{48}$$

$$\tau_i = \tau_{\text{eq}} = \frac{\delta}{3} \tag{49}$$

Moreover the bulk and surface current densities j_s and j_b vanish. By using Eqs. 39 and 43, one gets

$$-K_{\text{fs}}x_{tpb}\left(\left[\text{Co}_{\text{Co}}^{\text{x}}\right]_1^2 + \left[\text{Co}_{\text{Co}}^{'}\right]_1^2\right) \\ + K_{\text{bs}}\left(1 - x_{tpb}\right)\left(\left[\text{Co}_{\text{Co}}^{\text{x}}\right]_1^2 + \left[\text{Co}_{\text{Co}}^{\cdot}\right]_1^2\right) = 0 \tag{50}$$

$$-K_{\text{fb}}(1 - \tau_1) + K_{\text{bb}}\tau_1 = 0 \tag{51}$$

By taking

$$\frac{\text{d}\tau_m}{\text{d}t} = 0 \tag{52}$$

and using Eqs. 46, 47, 48 and 49 one gets

$$-K_{\text{in}}x\tau_{\text{eq}}\left(\left[\text{Co}_{\text{Co}}^{\text{x}}\right]_m^2 + \left[\text{Co}_{\text{Co}}^{'}\right]_m^2\right) \\ + K_{\text{out}}(1 - x)\left(1 - \tau_{\text{eq}}\right)\left(\left[\text{Co}_{\text{Co}}^{\text{x}}\right]_m^2 + \left[\text{Co}_{\text{Co}}^{\cdot}\right]_m^2\right) = 0 \tag{53}$$

By combining Eqs. 32 and 53 as well as Eqs. 40 and 50, one gets:

$$x = x_{\text{tpb}} = x_{\text{eq}} = \frac{\sqrt{K_{\text{ads}}p_{\text{O}_2}}}{\sqrt{K_{\text{ads}}p_{\text{O}_2}} + \sqrt{K_{\text{des}}}} \tag{54}$$
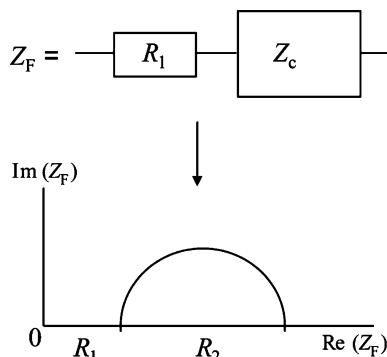

Fig. 4 Structure of the faradaic impedance Z_{F} of the reaction model. Z_{F} is composed of the charge transfer resistance R_1 and the concentration Z_{c}

The substitution of Eq. 54 into Eq. 53 leads to

$$K_{\text{in}} = \frac{3 - \delta}{\delta}\frac{\sqrt{K_{\text{des}}}}{\sqrt{K_{\text{ads}}p_{\text{O}_2}}}\frac{\left[\text{Co}_{\text{Co}}^{\text{x}}\right]_{\text{eq}}^2 + \left[\text{Co}_{\text{Co}}^{\cdot}\right]_{\text{eq}}^2}{\left[\text{Co}_{\text{Co}}^{\text{x}}\right]_{\text{eq}}^2 + \left[\text{Co}_{\text{Co}}^{'}\right]_{\text{eq}}^2}K_{\text{out}} \tag{55}$$

5.6 Choice of the reference potential

The equilibrium potential of the electrode/electrolyte interface is set to 0 by convenience. By using Eqs. 36, 37, 41, 42, 49, 50 and 51, this choice of a reference potential has the following consequences:

$$-k_{\text{fs}}x_{\text{eq}}\left(\left[\text{Co}_{\text{Co}}^{\text{x}}\right]_{\text{eq}}^2 + \left[\text{Co}_{\text{Co}}^{'}\right]_{\text{eq}}^2\right) \\ + k_{\text{bs}}\left(1 - x_{\text{eq}}\right)\left(\left[\text{Co}_{\text{Co}}^{\text{x}}\right]_{\text{eq}}^2 + \left[\text{Co}_{\text{Co}}^{\cdot}\right]_{\text{eq}}^2\right) = 0 \tag{56}$$

$$-k_{\text{fb}}\left(1 - \tau_{\text{eq}}\right) + k_{\text{bb}}\tau_{\text{eq}} = 0 \tag{57}$$

which leads to:

$$k_{\text{bs}} = \frac{x_{\text{eq}}}{1 - x_{\text{eq}}}\frac{\left[\text{Co}_{\text{Co}}^{\text{x}}\right]_{\text{eq}}^2 + \left[\text{Co}_{\text{Co}}^{'}\right]_{\text{eq}}^2}{\left[\text{Co}_{\text{Co}}^{\text{x}}\right]_{\text{eq}}^2 + \left[\text{Co}_{\text{Co}}^{\cdot}\right]_{\text{eq}}^2}k_{\text{fs}} \tag{58}$$

$$k_{\text{bb}} = \frac{3 - \delta}{\delta}k_{\text{fb}} \tag{59}$$

6 Simulations of faradaic impedances

6.1 General features

The structure of the faradaic impedance Z_{F} is

$$Z_{\text{F}} = R_1 + Z_{\text{c}}(\omega) \tag{60}$$

where ω is the angular frequency, $Z_{\text{c}}(\omega)$ is the concentration impedance and R_1 is the charge transfer resistance [22]:

$$\left(\frac{\partial j}{\partial E}\right)_{\tau_i, x, x_{tpb}} = \frac{1}{R_1} \tag{61}$$

The corresponding spectrum in the complex plane is schematically depicted in Fig. 4.

The resistance R_2 is the projection of $Z_{\text{c}}(\omega)$ on the real axis in the complex plane. The polarization resistance R_{p} is defined as

$$R_{\text{p}} = R_1 + R_2 \tag{62}$$

Table 3 Rate constants for kinetics with a single rate-determining step.

rds	Charge transfer	Adsorption	Incorporation	Diffusion
K_{ads} (mol^{-1} m^2 atm^{-1} s^{-1})	10^{13}	10^{8}	10^{13}	10^{13}
K_{des} (mol^{-1} m^2 s^{-1})	10^{13}	10^{8}	10^{13}	10^{13}
K_{out} (mol^{-3} m^9 s^{-1})	10^{-7}	10^{-7}	10^{-12}	10^{-7}
D (m^2 s^{-1})	10^{-8}	10^{-8}	10^{-8}	10^{-13}
k_{fb} (m s^{-1})	10^{-8}	10^{-2}	10^{-2}	10^{-2}
k_{fs} (mol^{-2} m^6 s^{-1})	10^{-7}	10^{-7}	10^{-7}	10^{-7}
K_s (C m^{-2})	10^{-7}	10^{-7}	10^{-7}	10^{-7}

6.2 Simulations

The electrochemical behaviour of the reaction model has been evaluated as a function of the electrode potential and thickness for various rds. The latter were defined by the relative values of the rate constants that can be found in Tables 3, 4 and 6. The other constants of the model are listed in Table 5. The numerical simulations were performed with the software package Matlab® 6.5/Simulink® 6 (Mathworks Inc.) using the toolboxes "Control System" (Version 5) and "Optimization" (Version 3).

6.3 Results

In the following and more specifically in the figure captions, the abbreviations "ads," "inc," "dif," "ctb" and "cts" stand for adsorption (rate constants K_{ads}, K_{des}), incorporation (K_{in}, K_{out}), diffusion (D), bulk charge transfer (K_{fb}, K_{bb}) and surface charge transfer (K_{fs}, K_{bs}), respectively. Due to the choice of the reference potential, this work deals only with negative values of E.

6.3.1 Bulk pathway

The kinetics and faradaic impedance of the bulk pathway can be individually studied when the contribution of the surface pathway is negligible (i.e. for low values of K_s and k_{fs}).

Charge transfer as single rds The overall oxygen reduction reaction is charge transfer limited when the supply of oxygen to the LSCF/CGO interface by adsorption, incorporation and bulk diffusion is fast enough in order to maintain the concentrations of oxygen vacancy and adsorbed oxygen at their equilibrium values (τ_{eq} and x_{eq}) regardless of the electrode potential. The concentration impedance vanishes ($R_2 \rightarrow 0$) and the impedance ($Z_F \sim R_1$) decreases with increasing $|E|$. The reaction follows a Butler–Volmer kinetics.

Adsorption, incorporation or diffusion as rds If a non-faradaic step is rate-determining, the charge transfer resistance vanishes ($R_1 \rightarrow 0$), i.e. $Z_F \sim Z_c$ and $R_p \sim R_2$. When adsorption or incorporation is rate-limiting, the concentration impedance describes a semi-circle in the complex plane. Adsorption-limited kinetics exhibits an increasing R_2 with increasing $|E|$ (Fig. 5). Conversely, when incorporation is the rds, R_2 decreases with $|E|$ (Fig. 6). When diffusion is rate-limiting, Z_F corresponds to a finite Warburg impedance (Fig. 7) with a typical 45° straight line at high frequency in the Nyquist plot.

However, in this work, due to numerical calculation (finite difference approach) used to implement the diffusion process, a deviation from the ideal Warburg behaviour at the intercept with the real axis is observed. This artefact could be corrected by increasing the number of compartments in the finite difference approach but this would significantly augment the calculation cost. In the following,

Table 4 Rate constants for kinetics with two rate-determining steps.

rds	Charge transfer and adsorption	Charge transfer and incorporation	Charge transfer and diffusion
K_{ads} (mol^{-1} m^2 atm^{-1} s^{-1})	10^{8}	10^{13}	10^{13}
K_{des} (mol^{-1} m^2 s^{-1})	10^{8}	10^{13}	10^{13}
K_{out} (mol^{-3} m^9 s^{-1})	10^{-7}	10^{-12}	10^{-7}
D (m^2 s^{-1})	10^{-8}	10^{-8}	$2\ 10^{-13}$
k_{fb} (m s^{-1})	10^{-8}	10^{-8}	10^{-8}
k_{fs} (mol^{-2} m^6 s^{-1})	10^{-7}	10^{-7}	10^{-7}
K_s (C m^{-2})	10^{-7}	10^{-7}	10^{-7}

Table 5 Fixed parameters of the reaction model.

Constants	Values
T (K)	873
p_{O_2} (atm)	0.21
α	0.5
N (mol m^{-2})	10^{-5}
m	9
EIS frequency range (Hz)	[$10^{-3}...10^{6}$] 8 points per decade
surface area of the LSCF electrode	3×3 mm^2

Table 6 Rate constants used in the simulations of Fig. 13.

rds	Bulk pathway	Bulk and surface pathways	Surface pathway
K_{ads} (mol^{-1} m^2 atm^{-1} s^{-1})	$5\ 10^8$	$5\ 10^8$	$5\ 10^8$
K_{des} (mol^{-1} m^2 s^{-1})	$5\ 10^8$	$5\ 10^8$	$5\ 10^8$
K_{out} (mol^{-3} m^9 s^{-1})	$2\ 10^{-10}$	$2\ 10^{-10}$	$2\ 10^{-10}$
D (m^2 s^{-1})	$2\ 10^{-12}$	$2\ 10^{-12}$	$2\ 10^{-12}$
k_{fb} (m s^{-1})	$5\ 10^{-8}$	$5\ 10^{-8}$	$5\ 10^{-8}$
k_{fs} (mol^{-2} m^6 s^{-1})	10^{-5}	10^{-5}	10^{-5}
K_s (C m^{-2})	10^{-2}	10	10^3

we considered that the diffusion impedance calculated with nine compartments constitute a good approximation. The faradaic impedance decreases with increasingly negative overpotentials (Fig. 7).

The relation $R_2-|E|$ is directly tied to the concentration of electroactive species. As shown in Fig. 8, in the case of adsorption as *rds*, the concentration of adsorbed oxygen quickly decreases with $|E|\left(\frac{d^2x}{d|E|^2}>0\right)$. This explains the apparition of a limiting current in the DC polarization curve and an increase of the polarization resistance. In contrast when the reaction is limited by incorporation or diffusion, the concentration of oxygen in the LSCF($1-\tau_i$) slowly decreases when one drifts away of the equilibrium $\left(\frac{d^2(1-\tau_i)}{d|E|^2}<0\right)$. This behaviour results from the relative contributions of the backward and forward steps in the charge transfer step (ratio k_{bb}/k_{fb}). When charge transfer is fast, the reaction remains at quasi-equilibrium. Using Eqs. 35, 36, 37 and 59, this leads to:

$$-k_{fb}e^{-2\alpha fE}(1-\tau_1)+k_{bb}e^{2(1-\alpha)fE}\tau_1 \approx 0 \tag{63}$$
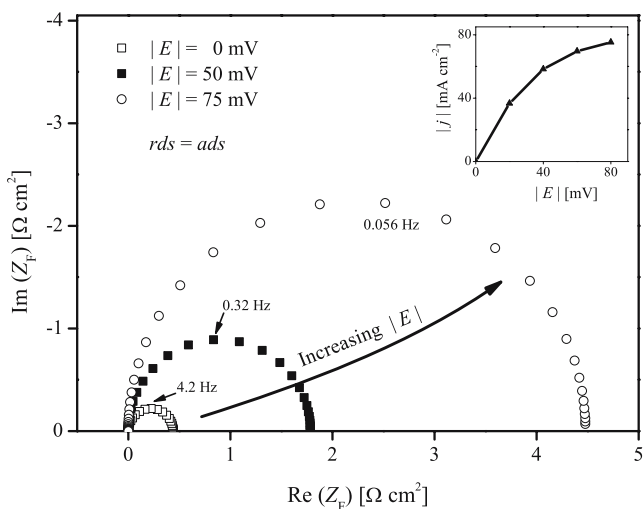
Fig. 6 Nyquist plots of the faradaic impedance Z_F for an incorporation-limited kinetics. The spectra have been calculated at $d=300$ nm. The insert shows the corresponding DC polarization curve. The relaxation frequencies are indicated on top of each impedance spectra
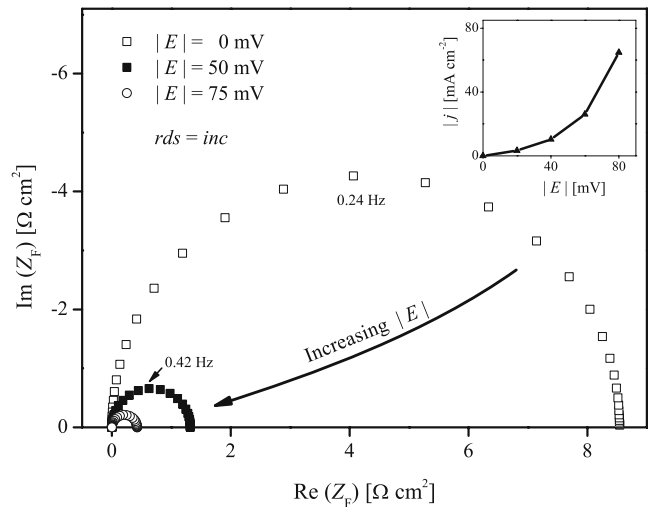
and

$$1-\tau_1 \approx \frac{\frac{k_{bb}}{k_{fb}}}{\frac{k_{bb}}{k_{fb}}+e^{2f|E|}} \approx \frac{\frac{3-\delta}{\delta}}{\frac{3-\delta}{\delta}+e^{2f|E|}} \tag{64}$$

In the LSCF, the oxygen concentrations $1-\tau_i$ are linearly dependent on $1-\tau_1$. The ratio $\frac{k_{bb}}{k_{fb}}$ is defined by Eq. 59. With $\delta=0.02$, $\frac{k_{bb}}{k_{fb}}=149$. This means that at low and moderate overpotentials, the anodic contribution (creation of oxygen in the LSCF) of the charge transfer step remains significant, which helps to maintain the oxygen concentration at the LSCF/CGO interface at a relatively high level and prevents the increase of the concentration impedance. As pointed out
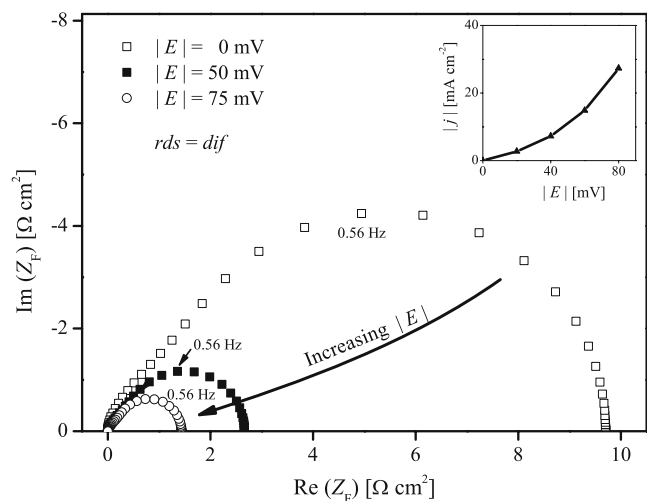
Fig. 5 Nyquist plots of the faradaic impedance Z_F for an adsorption-limited kinetics. The spectra have been calculated at $d=300$ nm. The insert shows the corresponding DC polarization curve. The relaxation frequencies are indicated on top of each impedance spectra
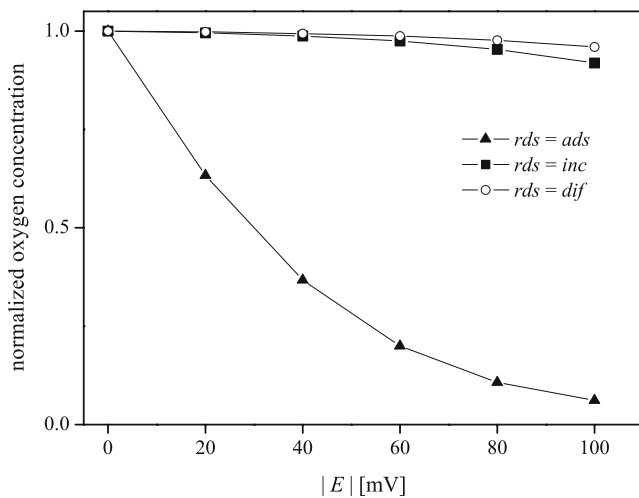
Fig. 7 Nyquist plots of the faradaic impedance Z_F for a diffusion-limited kinetics. The spectra have been calculated at $d=300$ nm. The insert shows the corresponding DC polarization curve. The relaxation frequencies are indicated on top of each impedance spectra

Fig. 8 Oxygen concentration dependence on the potential E as a function of the *rds*. The normalized concentration (with respect to the equilibrium) is: $\frac{x}{x_{eq}}$ for adsorption-limited kinetics (▲), $\frac{1-\tau_9}{1-\tau_{eq}}$ for incorporation-limited kinetics (■) and $\frac{1-\tau_5}{1-\tau_{eq}}$ for diffusion-limited kinetics (○)

Fig. 10 Nyquist plots of the faradaic impedance Z_F for kinetics limited by charge transfer (*ctb*) and one non-faradaic step (adsorption, incorporation or diffusion). The spectra have been calculated at $E=$ -100 mV and $d=300$ nm. The relaxation frequencies are indicated on top of each impedance spectra

in Fig. 9, this trend is inverted only for much lower values of $\frac{k_{bb}}{k_{fb}}$ (<4) which corresponds to unrealistic values of the oxygen nonstoichiometry ($\delta \sim 0.6$) in air at 600°C.

Charge transfer and one non-faradaic step as rds When charge transfer and a non-faradaic step are rate-limiting, both R_1 and R_2 are of the same order of magnitude (Fig. 10). The shape of the concentration impedance is qualitatively the same as described in the previous paragraph. R_1 and R_2 depend on the electrode potential. When R_1 is greater than R_2, the latter tends to decrease with the potential. When R_1 becomes small, the variations of R_2

with E are similar to the case described above ("*Adsorption, incorporation or diffusion as rds*").

Several non-faradaic steps as rds Several non-faradaic steps may be simultaneously rate-determining. The shape of the resulting faradaic impedance is a "combination" of the frequency response of the kinetics limited by one *rds* only.

When adsorption and incorporation are rate-determining, Z_F can be described with one semi-circle in the complex plane. The variation of R_p with respect to $|E|$ depends on the preponderance of one or the other step. When diffusion is rate-limiting with either adsorption or incorporation, the 45° line at high frequency typical of the Warburg impedance progressively vanishes when the diffusion coefficient D increases, i.e. when diffusion becomes faster (Fig. 11). The shape of the concentration impedance does not vary whether charge transfer is limiting or not. The same qualitative results are obtained when all the reaction steps (adsorption, incorporation, diffusion and charge transfer) are rate-determining.

Influence of the electrode thickness The contribution of diffusion to the overall kinetics can be evidenced by studying the dependence of R_p on the electrode thickness d ($R_p \propto d^n$). As illustrated in Fig. 12, when the reaction is limited by diffusion only, a linear dependence ($n=1$) exists between the polarisation resistance and the electrode thickness. When diffusion is only one of the *rds*, the dependence on d is reduced ($0<n<1$). When diffusion is a fast step, n becomes 0.
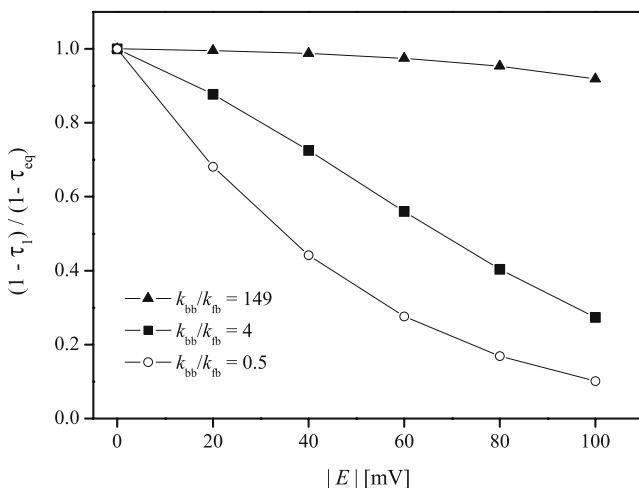

Fig. 9 Dependence of the normalized oxygen concentration $\frac{1-\tau_1}{1-\tau_{eq}}$ on the potential E as a function of the *kfb/kbb* ratio when charge transfer remains at quasi-equilibrium
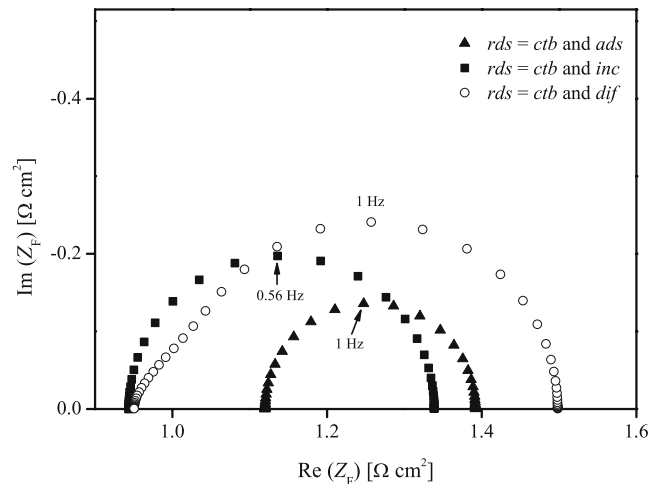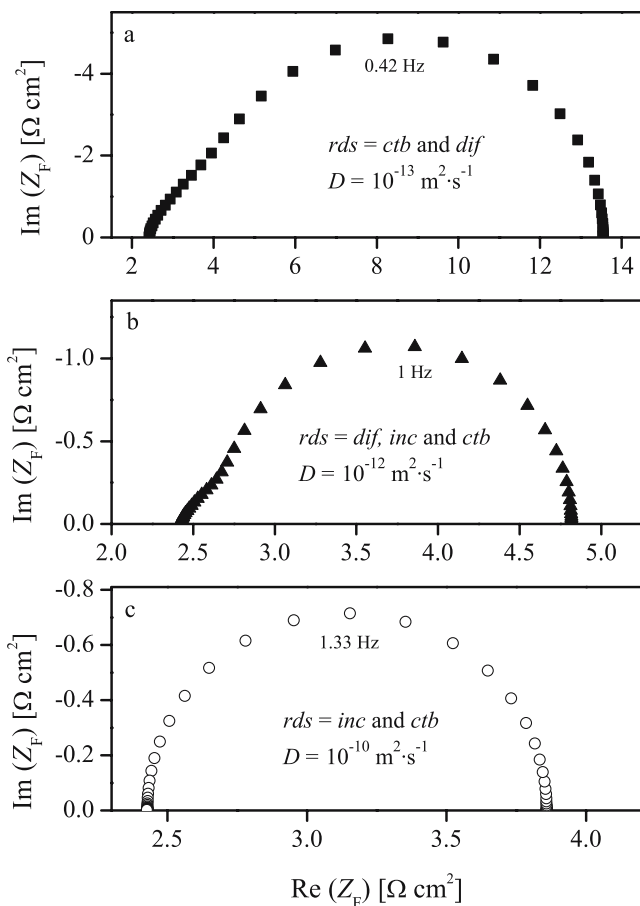
Fig. 11 Nyquist plots of the faradaic impedance Z_F for kinetics limited by charge transfer (*ctb*), diffusion and incorporation. The shape of Z_F varies from a Warburg impedance (**a**) to a semi-circle (**b**) when the diffusion coefficient is increased. The other rate constants are fixed: $K_{ads}=10^{13}$ mol^{-1} m^2 atm^{-1} s^{-1}, $K_{des}=10^{13}$ mol^{-1} m^2 s^{-1}, $K_{out}=6\ 10^{-12}$ mol^{-3} m^9 s^{-1}, $k_{fb}=10^{-8}$ m s^{-1}, $k_{fs}=10^{-7}$ mol^{-2} m^6 s^{-1} and $K_s=10^{-7}$ C m^{-2}. The spectra have been calculated at $E=0$ mV and $d=300$ nm. The relaxation frequencies are indicated on top of each impedance spectra

Fig. 12 Dependence of the polarisation R_p on the electrode thickness d when diffusion and charge transfer (*ctb*) are rate-determining

K_s is related to the geometry electrode:

$$K_s = \frac{2Fl_{tpb}wN}{A} \qquad (65)$$

whereby l_{tpb} is the *tpb* length (i.e. the perimeter of the square-shaped electrode), w the *tpb* width and A the surface area of the electrode $\left(A = \frac{l_{tpb}^2}{16}\right)$.

With geometrically well-defined electrodes, l_{tpb} and A are easily controllable. However, w is vaguely known. w can be considered as the diameter of an oxygen atom (0.121 nm). It seems unlikely that w is orders of magnitude bigger than this value. For a 3×3 mm^2 electrode, K_s ranges between 10^{-6} and 10^{-7} C m^{-2}. The values of K_s that lead to

Therefore in impedance experiments the electrode thickness, i.e. the diffusion length, constitutes a major and easily controllable parameter to investigate the contribution of the bulk pathway.

6.3.2 Competition between surface and bulk pathways

In the present reaction model, the bulk and surface pathways are parallel, i.e. in competition. The rate-determining pathway is the one with the fastest kinetics. The kinetics of the surface pathway is dependant on the rate constant k_{fs} and on K_s. Fig. 13 illustrates the influence of the surface pathway on the faradaic impedance spectra. The different kinetic situations have been calculated by varying the value of K_s (see Table 6).
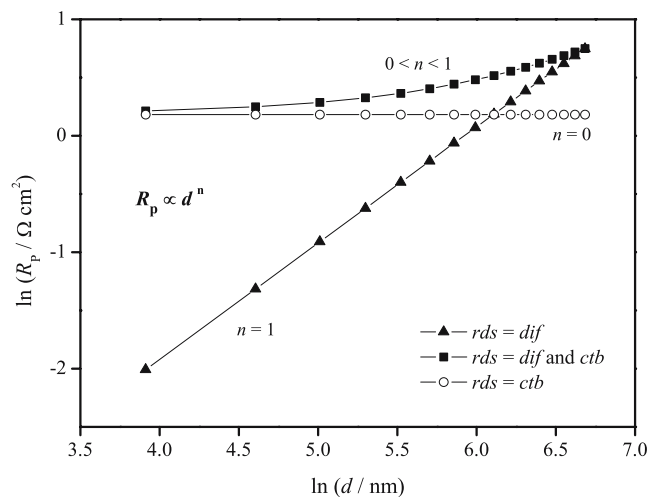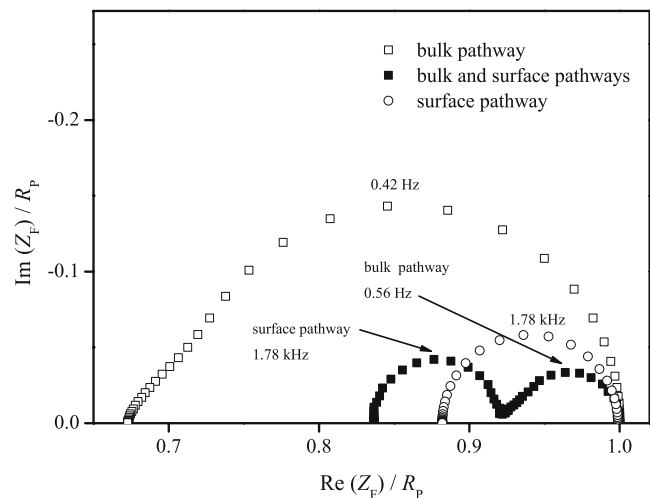

Fig. 13 Normalized Nyquist plots of the faradaic impedance Z_F whereby the overall kinetics of the oxygen reduction reaction is determined by the bulk and surface pathways. The contribution of the surface pathway has been modified by varying K_s. The spectra have been calculated at $E=-100$ mV and $d=300$ nm. The relaxation frequencies are indicated on top of each impedance spectra

a surface pathway competitive with the bulk pathway (see Fig. 13) are far above this estimate. The surface pathway may also be rate-determining with fast charge transfer (high k_{fs}) while keeping K_s at a reasonable value (10^{-6}–10^{-7} C m^{-2}). However this would significantly deplete the *tpb* of adsorbed oxygen and limit the surface current density j_s. Moreover with such large and unrealistic values of k_{fs}, the faradaic impedance would be shifted to higher frequencies than the ones used in impedance spectroscopy. Consequently the contribution of the surface pathway is not believed to play a significant role in the overall oxygen reduction kinetics at thin dense LSCF electrodes.

6.3.3 Capacitive effects

When at least one of the non-faradaic steps of the reaction is rate-limiting, Z_F exhibits a capacitive behaviour that originates from the concentration impedance. For instance, when adsorption or incorporation is the *rds*, the concentration impedance can be represented by a semi-circle that includes a faradaic capacitance. The latter must be differentiated from a double layer capacitance that does not depend on the reaction kinetics in first approximation. In order to compare experimental and simulated impedances, Z_F is incorporated in an equivalent circuit accounting for the electrolyte impedance Z_e and the double layer capacitance C_{DL} at the electrode/electrolyte interface (Fig. 14). The latter can be represented either as a pure capacitance or a so-called constant phase element (CPE). The overall simulated impedance is denoted Z_{SIM}.

Z_{SIM} is strongly influenced by the interaction between C_{DL} and C_F as illustrated in Fig. 15. When C_{DL} is low, Z_{SIM} ~ Z_F. When C_{DL} is moderate, a semi-circle resulting from
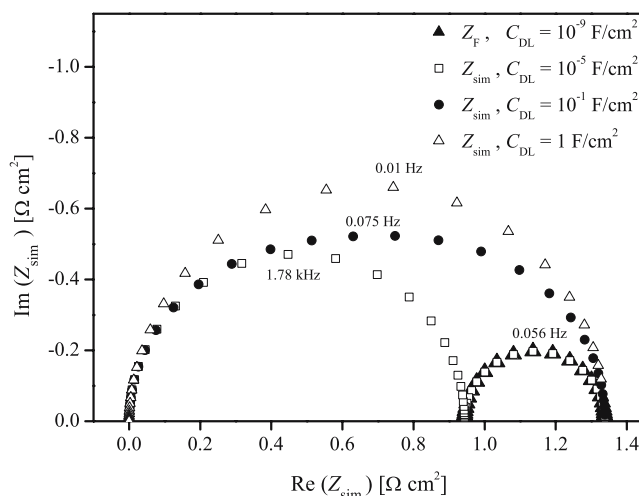
Fig. 15 Total simulated impedance Z_{SIM} as a function of the double layer capacitance C_{DL} when incorporation and charge transfer (*ctb*) are rate-determining. The faradaic impedance was calculated at $E=$ -100 mV and $d=300$ nm. The relaxation frequencies are indicated on top of the impedance spectra

the coupling between R_1 and C_{DL} between appears at high frequency while at low frequency, Z_{SIM} ~ Z_F. For large C_{DL} the charge transfer resistance and the concentration impedance are partially or totally masked by the double layer capacitance and cannot be distinguished anymore. In this work, the simulations based on realistic values of the rate constants and impedances show that the faradaic capacitances are quite high (around 0.1–1 F cm^{-2}) which is good agreement with theoretical and experimental findings of Adler et al. [5]. It seems therefore unlikely that Z_F can be masked by double layer capacitances (~10^{-4}–10^{-6} F cm^{-2}).

7 Discussion

The simulations have shown that the faradaic impedance Z_F and its variations as a function of electrode potential and thickness exhibit typical features depending on the *rds*. This illustrates the necessity of a modelling approach preliminary to the investigation of experimental impedance spectra. It was demonstrated that thin dense LSCF electrodes promote oxygen reduction along the bulk pathway. These findings are in good agreement with the work of Brichzin [9] who observed the same phenomenon at thin dense LSM electrodes despite the fact that this compound exhibits low bulk transport properties of oxygen compared to LSCF [11, 12]. The small surface contribution of our electrodes can be easily explained by the limited *tpb* length, 13 cm^{-1} for a 3× 3 mm^2 dense electrode of this study instead of *ca*. 10^4 cm^{-1} typically for conventional porous electrodes. Increasing the *tpb* length is possible by microstructuring the electrode into stripes as reported by Bieberle and Gauckler [23]. However,
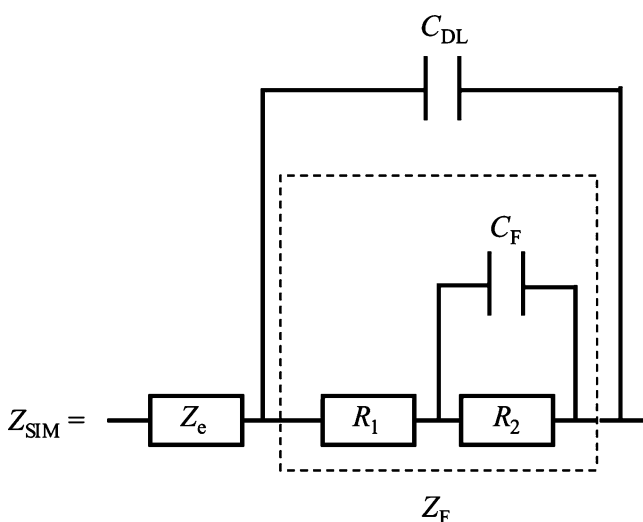

Fig. 14 Equivalent circuit for the total simulated impedance Z_{SIM}. In this example, the reaction kinetics, represented by Z_F, is limited by charge transfer and adsorption or incorporation

with today's photolithographic techniques, the minimal width of stripes of LSCF is not expected to be smaller than 10 µm. The resulting *tpb* length would be increased only by a factor of 100. Moreover small stripe width would question the assumption (14) of the model that stipulates that the contribution of oxygen exchange at the lateral planes (*xz*) and (*yz*) (see Fig. 3) can be ignored. The electrochemical process currently seen as a one-dimensional process along the *z* axis in this work would require an additional dimension.

The kinetics of an electrochemical process is determined by the relative values of the rate constants of the single steps. If one of the kinetic parameters is known, even roughly, all the other rate constants of the model can be estimated (if they are rate-determining). In the case of oxygen reduction at thin dense LSCF electrodes, where the bulk pathway is predominant, the investigation of the reaction kinetics can make use of reliable literature information on oxygen diffusivity [8, 21, 24, 25] as well as oxygen exchange coefficient [8, 24, 25]. These data are mainly obtained from independent techniques such as isotope exchange depth profile (IEDP) [26, 27] and conductivity relaxation [28]. The oxygen vacancy diffusivity D can be estimated from the oxygen self diffusion coefficient D_O by using the relation:

$$C_V D = C_O D_O. \tag{66}$$

whereby C_O and C_V is the concentration of oxygen and oxygen vacancies at equilibrium respectively [25].

In the IEDP technique the surface exchange coefficient k is defined by

$$k = \frac{J_O}{C_O} \tag{67}$$

with J_O being the flux of oxygen crossing the gas/oxide interface. Consequently, in the present reaction model, the rate constant K_{out} can be related to k:

$$k \approx K_{out} N \left(1 - x_{eq}\right) \left(\left[Co_{Co}^x\right]_{eq}^2 + \left[Co_{Co}^{\cdot}\right]_{eq}^2 \right) \tag{68}$$

The fact that D and K_{out} can be estimated make possible an approximated assessment of the other rate-determining constants, even the most poorly known ones such as K_{ads}, K_{des}, k_{fb} and k_{bb}, (see Tables 3 and 4).

A defect chemistry model was used to account for the variations of charge distribution when the oxygen concentration in the bulk of LSCF changes out of equilibrium. In this work, the vacancy concentrations remained in the acceptable physical range of the model ($\tau_i < 0.24$). To the best of our knowledge, no description is available in the field of thermodynamic modelling concerning the defect chemistry of LSCF in a more reduced state. It would be of great interest to investigate the effect of reducing conditions on the LSCF layer in order to figure out how it may decompose into primary oxides and if low oxygen content may lead to the formation of new internal structure as already reported for other perovskites [29–31].

The influence of temperature on the faradaic impedance has not been reported in this paper. The proposed model is valid for temperatures at which the LSCF layers exhibits oxygen vacancies to achieve the diffusion process. Within the range of validity of the model, the qualitative results of this study are not influenced by the choice of the temperature while quantitatively the impedance is expected to increase with decreasing temperature.

8 Conclusions and outlook

A reaction model for oxygen reduction at thin dense mixed-conducting $La_{0.52}Sr_{0.48}Co_{0.18}Fe_{0.82}O_{3-\delta}$ electrode has been investigated by calculating its faradaic impedance. The reaction mechanism consists of a bulk pathway and a surface pathway in parallel. Adsorption, oxygen incorporation, diffusion and charge transfer constitutes the bulk pathway. The model takes the defect chemistry of the LSCF film into account as well. The relation between the faradaic impedance and the reaction kinetics has been examined by varying the rate constants of the model. It has been demonstrated that the rate-determining steps of the reaction can be identified by the specific features exhibited by the faradaic impedance.

Useful information concerning the reaction mechanism can be obtained by examining the variation of the faradaic impedance with the electrode potential and thickness. In particular, the effect of bulk diffusion of oxygen has been evidenced by measuring the change of the polarisation resistance upon varying the electrode thickness. The simulations show that the contribution of the surface pathway is negligible for electrode with such small triple phase boundary length. The faradaic impedance exhibits a high capacitive effect that may overcome the "masking" effect of double layer capacitance observed in other SOFC cathodic systems.

In a companion paper [16], oxygen reduction at the $La_{0.52}Sr_{0.48}Co_{0.18}Fe_{0.82}O_{3-\delta}$/CGO interface is experimentally investigated by means of impedance spectroscopy. The thin dense LSCF films has been prepared by pulsed laser deposition and structured with photolithography. The impedance of the reaction has been measured as a function of electrode potential. Varying the LSCF film thickness has been used to evidence the eventual role of diffusion in the reaction kinetics. The collected experimental data has been confronted to the reaction model studied in the present work.

101

References

1. L.J. Gauckler, D. Beckel, B.E. Buergler, E. Jud, U.P. Muecke, M. Prestat, J.L.M. Rupp, J. Richter, Chimia **58**, 837 (2004)
2. S.P. Jiang, Solid State Ion. **146**, 1 (2002)
3. F.M. Figueiredo, J.A. Labrincha, J.R. Frade, F.M.B. Marques, Solid State Ion. **101–103**, 343 (1997)
4. S.B. Adler, Chem. Rev. **104**, 4791 (2004)
5. S.B. Adler, J.A. Lane, B.C.H. Steele, J. Electrochem. Soc. **143**, 3554 (1996)
6. M. Liu, Z. Wu, Solid State Ion. **107**, 105 (1998)
7. J.D. Sirman, J.A. Lane, J.A. Kilner, in *Ionic and Mixed Conducting Ceramics III*, ed. by T.A. Ramanarayanan, W.L. Worell, H.L. Tuller, A.C. Khandkar, M. Mogensen, W. Gopel (The Electrochemical Society, PV 97-24, Pennington NJ, 1997), p. 57
8. B.C.H. Steele, J.-M. Bae, Solid State Ion. **106**, 255 (1998)
9. V. Brichzin, J. Fleig, H.-U. Habermeier, J. Maier, Electrochem. Solid-State Lett. **3**, 403 (2000)
10. F. Baumann, J. Fleig, J. Maier, in *Proceedings of the 6th European Solid Oxide Fuel Cell Forum*, ed. by M. Mogensen (Lucerne, Switzerland, 2004), p. 1241
11. R.A. De Souza, J.A. Kilner, J.F. Walker, Mater. Lett. **43**, 43 (2000)
12. R.A. De Souza, J.A. Kilner, Solid State Ion. **126**, 153 (1999)
13. A. Esquirol, N.P. Brandon, J.A. Kilner, M. Mogensen, J. Electrochem. Soc. **151**, A1847 (2004)
14. A. Mitterdorfer, L.J. Gauckler, Solid State Ion. **117**, 187 (1999)
15. A. Mitterdorfer, L.J. Gauckler, Solid State Ion. **117**, 203 (1999)
16. M. Prestat, A. Infortuna, S. Korrodi, S. Rey-Mermet, P. Muralt, L.J. Gauckler, J. Electroceramics, in press (2007)
17. S. Wang, M. Katsuki, M. Dokiya, T. Hashimoto, Solid State Ion. **159**, 71 (2003)
18. D. Waller, J.A. Lane, J.A. Kilner, B.C.H. Steele, Solid State Ion. **86–88**, 767 (1996)
19. A.L. Shaula, V.V. Kharton, F.M.B. Marques, J. Eur. Ceram. Soc. **24**, 2631 (2004)
20. L.-W. Tai, M.M. Nasrallah, H.U. Anderson, D.M. Sparlin, S.R. Sehlin, Solid State Ion. **76**, 273 (1995)
21. J.W. Stevenson, T.R. Armstrong, R.D. Carneim, L.R. Pederson, W.J. Weber, J. Electrochem. Soc. **143**, 2722 (1996)
22. J.-P. Diard, B. Le Gorrec, C. Montella, *Cinétique Electrochimique* (Hermann, Paris, France, 1996) p. 202
23. A. Bieberle, L.J. Gauckler, Solid State Ion. **146**, 23 (2002)
24. S.J. Benson, R.J. Chater, J.A. Kilner, in *Solid Oxide Fuel Cells V*, ed. by H. Yokokawa, S.C. Singhal (The Electrochemical Society, PV 1997-24, Pennington, NJ 1997), p. 596
25. M. Katsuki, S. Wang, M. Dokiya, T. Hashimoto, Solid State Ion. **156**, 453 (2003)
26. R.J. Chater, S. Carter, J.A. Kilner, B.C.H. Steele, Solid State Ion. **53–56**, 859 (1992)
27. J.A. Kilner, R.A. De Souza, I.C. Fullarton, Solid State Ion. **86–88**, 703 (1996)
28. J.A. Lane, J.A. Kilner, Solid State Ion. **136–137**, 997 (2000)
29. E. Bucher, W. Sitte, I. Rom, I. Papst, W. Grogger, F. Hofer, Solid State Ion. **152–153**, 417 (2002)
30. R.H.E. van Doorn, A.J. Burggraaf, Solid State Ion. **128**, 65 (2000)
31. A.N. Petrov, O.F. Kononchuk, A.V. Andreev, V.A. Cherepanov, P. Kofstad, Solid State Ion. **80**, 189 (1995)